Seismic noise tomography in regions with small velocity contrasts and strong noise directivity: application to the northern Baltic Shield

Piero Poli, M. Campillo, Helle A. Pedersen

Seismic noise tomography in regions with small velocity contrasts and strong noise directivity: application to the northern Baltic Shield

P. Poli[1], M. Campillo[1], H. A. Pedersen[1] , and the POLENET/LAPNET Working Group

1-ISTerre, Université de Grenoble I, CNRS, BP 53, F-38041 Grenoble Cedex 9, France

Abstract

Ambient noise tomography (ANT) is widely used to image strong velocity variations within the upper crust . Using careful processing, we obtained a 3-D model of shear velocities in the upper crust beneath northern Finland, where the lateral velocity variations are less than 3%. As part of the tomography, the noise field is analysed. It is strongly heterogeneous but the signal to noise ratio is sufficient to obtain stable dispersion curves for all profile azimuths. Our results show that the directions of dominant noise sources of Rayleigh and Love waves are the same, but the amplitude distribution with azimuth is different for the two types of waves. More intriguingly, the high frequency Love waves are dominated by a mixture of higher modes rather than the fundamental mode. The reconstructed 3-D model shows the Lapland Granulite Belt as a high velocity body with a limit at surface in excellent agreement with geological observations at surface. Following this interface at depth, our results are compatible with previous studies suggesting an archean north oriented subduction.

1-Introduction

Ambient Noise Tomography (ANT) is a recently developed branch of seismology for which one major application is crust and upper mantle surface wave tomography. Instead of relying in the presence of transient sources, ANT is based on correlation of a

25 random wave-field to extract the Green's function (Campillo and Paul, 2003, Shapiro and
26 Campillo, 2004, Sabra et al. 2005a, Pedersen et al., 2007, Gouédard et al., 2008). With
27 this technique, it is possible to overcome a series of classical problems in surface wave
28 tomography, in particular the lack of homogeneous distributed transient sources, and
29 the difficulty of extracting the high frequency part of dispersion curves in the case of
30 distant sources. ANT is however not free of difficulties, related to the distribution of the
31 noise sources. Firstly, the sources are mainly located at the surface. This may actually be
32 an advantage to ANT as the extracted records are dominated by surface waves.
33 Secondly, as the noise sources are unevenly distributed at the surface (Stehly et al.,
34 2006) the observed surface wave velocities may be biased (Pedersen et al., 2007, Yao et
35 al., 2009, Froment et al., 2010).
36 Spectacular applications can be fund all over the world (e. g. Shapiro et al., 2005, Sabra
37 et al., 2005b, Stehly et al. 2009, Ritzwoller et al., 2011). Most studies have focused on
38 areas with strong velocity variations (typically up to ± 5-20%), as those observed
39 between sediments and bedrock. In such cases the possible bias and/or lack of precision
40 in dispersion measurements using estimated Green's functions is smaller than the
41 retrieved velocity variations in the model, and high-resolution tomography is robust, as
42 shown by the similar results obtained by the two independent studies of Sabra et al.
43 (2005b) and Shapiro et al. (2005).
44 In the absence of sediments or if the crustal rock composition does not vary significantly
45 across the study area, seismic velocities typically vary less than ±3 %. Examples of such
46 challenging areas are cratons, which are presently subject to much attention as a key to
47 understanding the evolution of the early Earth, and due to their strategic role for ore
48 exploration. In this case, the lateral velocity variations may be smaller than the errors
49 associated with ANT, so particular care must be taken during all processing steps to

achieve a good signal to noise ratio for a wide range of azimuths. Recently, Prieto et al. (2011) and Poli et al. (2012) demonstrated that using small time windows is a more efficient way to ensure a good Green's function estimation than using 1-day time windows. These studies show that there are still significant improvements in ANT through refining the processing methods.

In this article we use ANT to obtain a 3D Vs model of northern Fennoscandia. This zone is a stable cratonic area where velocity variations from previous models are in the range of ±3% or less (Janik et al., 2009). The complex geometry of tectonic units at the surface, leading to a variety of models for the tectonic evolution of the area, does not translate into lateral major velocity variations in the crust. The only 'major' velocity contrast observed on 2-D active seismic profiles is created by a high velocity upper crustal body (+3%) which is interpreted as a remnant slice of Archean crust, related with an Archean subduction event (Janik et al., 2009, and reference therein).

We firstly present the processing that we apply, after which we analyse the directivity of the noise field and the modal composition of the extracted surface waves. Special attention was given to the extraction of Love waves, as they give complementary information to the Rayleigh waves through different sensitivity, and insight to radial anisotropy. In this study we bring some additional understanding of the origin of these difficulties as the absence of sedimentary basins facilitates the interpretation of the observed Love wave. We subsequently measure group velocities for all station profiles and calculate group velocity maps for a series of frequencies. These group velocity maps are used as input to an inversion aimed at the 3-D model of shear velocities.

2-DATA PROCESSING AND NOISE WAVE-FIELD

We analyse seismic data continuously recorded during the POLENET/LAPNET temporary experiment (Kozlovskaya et al., 2006) in northern Fennoscandia. The array configuration (fig. 1) is approximately a 2D grid with station separations that span from ~50 km to ~600 km. We used records for the calendar year 2008 during which the array was fully operational. Standard preprocessing was applied, including removing mean and data trend, pre-filtering, resampling to identical sample rate (5 hz) and deconvolution of the instrumental responses. In this section we present in some detail the processing used to estimate the Green's function after which we present the characteristics of the noise field.

2.1-Green's function estimation

To be able to extract Rayleigh and Love waves we calculated ZZ and TT noise cross-correlations using vertical-vertical and transverse-transverse (TT) components. Since our goal was to obtain a good estimation of the Green's function, we compared the result of a series of processing methods, for which we present the main results. Poli et al. (2012) used a processing procedure which effectively made it possible to extract the body wave part of the Green's function. Different from standard noise correlation processing, they used short time windows (4 hours) and pre-whitening of the data. No time domain (e. g. one-bit) normalization was applied, but all time windows were statistically analyzed and removed if amplitudes larger than 10 times the standard deviation of the data were fund. This approach was used to reduce the effect of transient sources and instrumental problems while obtaining a broadband correlation.

To quantify the benefit of using this processing we compared the resulting noise correlations with noise correlations obtained using 1-bit normalization, and using linear correlation without pre-whitening. In both cases we used the same rejection criteria of windows with high amplitudes. We here show the results using vertical component data from two stations located approximately 200 km apart. Two parameters were defined to estimate the quality of the obtained Rayleigh wave GF. The correlation coefficient ('*R*') provides the convergence rate in time (months) towards a reference correlation function *ref*:

$$R(j) = \frac{\Theta(j,ref)}{\sqrt{\Theta(ref,ref)\Theta(j,j)}} \quad (109)$$

where Θ (j,ref) is the correlation between correlation j and the reference correlation *ref*, and C(j,j) and C(ref,ref) are their autocorrelations. Here *ref* is the reference correlation (averaged over 12 months) and *j* the correlation function averaged over months 1 to *j*. The Signal to Noise Ration ('*SNR*') defines how the Greens function's emerge from the remnant oscillations of the noise:

$$SNR(j) = \frac{\max(signal(j))}{rms(noise(j))}$$

where *Signal(j)* is the correlation function within the time window delimited by group velocities 3 and 4 km/sec and *Noise(j)* is the 1000 sec tail of the correlation function. In both Signal(j) and Noise(j) the correlation function is stacked over months 1 to j. SNR is averaged over the causal and acausal part.

Figure 2 shows *R(j)* and *SNR(j)* for the different types of processing. Firstly, we evaluate the benefit obtained by using 4 hours time windows as compared to 24 hours time windows. For both R (fig. 2-a) and SNR (fig. 2-b) we observe that correlations calculated with shorter time windows (green lines) converge significantly more rapidly than for longer time windows (green dashed lines) and that the signal to noise ratio is improved approximately by a factor of two.

The comparison of R and SNR for the processing of Poli et al. (2012) using 4 hour windows (green lines) with one-bit correlation (blue lines) and linear correlation (red lines), calculated using 4 hour windows shows that the former provides a faster rate of convergence, with a SNR twice the one observed for one-bit or linear correlations. Following these results, we proceeded to the calculation of the noise correlation as in Poli et al. (2012).

2.2-Directivity of seismic noise

Since the SNR of the correlations is an estimate of the coherent surface wave energy contained in the noise wave-field, we use SNR to provide insight to the azimuth distribution of the incoming noise in different frequency bands.

In figure 3, the SNR for Love (blue lines) and Rayleigh (red lines) waves is reported as a function of azimuth, and for the period ranges 10-20s (Fig. 3-a) and 2-10s (Fig. 3-b). The

148 SNR value is evaluated every 10° of azimuth, by averaging the SNR over a sliding 10°
149 wide non-overlapping azimuth window. Individual traces may therefore have a smaller
150 SNR than that reported onto this figure.
151
152 At long period (fig 3-a), Rayleigh waves have high SNR for most azimuths, with a clear
153 decrease of SNR towards the S-SE and a minimum SNR, of approximately ten, between
154 100° and 200°. The Love waves also have a minimum in this azimuth interval, but SNR is
155 significantly higher towards the west than towards the east.
156
157 At short period (fig 3-b), Rayleigh waves have a similar pattern as for long periods, but
158 SNR are different by a factor of two towards south to west (SNR<150) as compared to
159 the east (SNR<70). Love waves on the other hand have a pattern opposite to what is
160 observed at long periods, with the highest SNR towards the east (SNR<50) and lowest
161 towards the west (SNR<25).
162 The overall low SNR towards the south can be explained by the large distance to
163 possible oceanic sources (Stehly et al., 2006) so wave attenuation plays a substantial
164 role in reducing the observed energy. On the other hand, the differences between Love
165 and Rayleigh waves do not have a straightforward explanation.
166 In spite of the variable SNR as a function of period, we consider SNR to be overall good,
167 as it is higher than 10 for all azimuths. We attribute the differences with Friederch et al.
168 (1998) and Pedersen et al. (2007), who mainly identified noise sources in the Atlantic
169 Sea, to the inclusion of the summer months in the analysis, and to the processing using
170 short time windows. The influence of the processing might explain the difference with
171 Kohler et al. (2011) who analysed noise correlations and source distribution in southern

172 Scandinavia. These authors used running absolute mean normalization over 15 minute
173 windows, and they used data from a 20 months recording period.
174 When we measure group velocities in narrow frequency bands, a large scatter is
175 however present for the azimuths with relatively low SNR. To avoid this problem, we
176 add the correlation traces of positive and negative times for each profile, prior to group
177 velocity analysis. Figure 4 shows that this procedure yields consistent group velocities
178 for all profile orientations, with only a small number of outliers, mostly for N-S oriented
179 profiles. There is no indication of systematic bias due to localized sources. The
180 improvement as compared to Pedersen et al. (2007), who showed strong azimuth
181 dependence for some frequencies, is likely to be due to a longer recording period in our
182 study, as we use 12 months of data, while Pedersen et al. only had data available from
183 the six months winter half year. The major implication of our noise directivity analysis
184 and the good to excellent SNR is that we can measure reliable dispersion curves for all
185 profile orientations.
186 In figure 5 we show the spectrogram of the correlations with the aim at understanding
187 which modes dominate the noise field. We used the two profiles, oriented N-S and E-W,
188 using the most distant stations available for these azimuths. For each profile we observe
189 that the ZZ component (figs 5-a and 5-c) is dominated by fundamental mode Rayleigh
190 waves. The TT component (figs 5-b and 5-d) shows a more complex behavior. At periods
191 larger than 10 sec, the TT component is dominated by fundamental mode Love waves,
192 while we observe a mix of higher modes at shorter periods. The sum of these higher
193 modes could be interpreted as Lg waves (e.g. Campillo, 1990).
194 Due to frequency-time analysis smoothing, the mix of higher modes of the Love waves is
195 not easily identified in more complex tectonic settings, so erroneous interpretation of
196 apparently continuous dispersion curves could easily occur. Our results show that the

use of Love waves at periods shorter than 10s may not be feasible in many cases. One implication of a misidentification of the mode associated with the high frequency part of the TT dispersion curve could be a Rayleigh-Love discrepancy, which would be interpreted as radial anisotropy of the upper crust. In our case, this apparent discrepancy would lead to approximately 4% anisotropy ($(V_{SH}-V_{SV})/ V_{SV}$) in the top 10km of the crust.

Once the periods shorter than 10s were discarded, the period interval over which we obtained reliable dispersion curves for the Love waves was too narrow to give any additional information to the inversion. We therefore focus the tomography on the analysis of the fundamental mode Rayleigh waves.

3-FROM NOISE CORRELATION TO GROUP VELOCITY MAPS

Once the periods shorter than 10s were discarded, the period interval over which we obtained reliable dispersion curves for the Love waves was too narrow to give any additional information to the inversion. We therefore here focus the tomography on the analysis of the fundamental mode Rayleigh waves as observed on the ZZ component. We firstly measure dispersion curves for all station pairs after which we invert these dispersion curves to obtain group velocity maps for the study region.

3.1-Dispersion measurements

Out of 861 ZZ correlation functions calculated, we retained the 745 with SNR ratio higher than 10 for either positive or negative times (or both). These correlations were averaged between the causal and acausal part prior to dispersion measurements. We used multiple filter analysis (Levshin et al., 1989) to automatically measure the group velocity dispersion curve. The fundamental mode Rayleigh wave was isolated using a

cosine time domain window centered on predicted group velocities from an average crustal model of the area (Poli et al., 2012).

Dispersion measurements were carried out in a period range of 1 to 50 sec. For each profile we excluded periods beyond which the profile length was smaller than two wavelengths. At periods longer than 25s, this criterion reduced the number of profiles to only the very longest ones, with a dominance of N-S oriented profiles, as the array dimension is bigger in this direction. We therefore decided to exclude periods longer than 25s from the tomography to avoid N-S smearing.

Finally, outliers where removed trough statistical analysis of the group velocity for each period. All velocity measurements that did not fall within two standard deviations of the mean (see also fig 4) were discarded.

3.2-Calculation of group velocity maps

We inverted our dispersion measurements following the tomographic approach proposed by Barmin et al. (2001), and we refer to this reference paper for a detailed description. The method is based on the minimization of a penalty function composed by a linear combination of data misfits, model smoothness and magnitude of perturbations. A priori parameters are defined to regularize the solution. The spatial smoothing is controlled by two parameters α and σ where σ defines the width of a Gaussian smoothing function and α is the weight given to the spatial smoothing term of the misfit function. The magnitude of the model perturbations is controlled by the parameter β and λ, the latter defining the weight of path density.

As we only analyse the results in the areas with good path coverage, the smoothing was mainly controlled by α and σ. After verifying that λ and β did not affect the final solution

247 in the well resolved parts of the model, they were set to respectively 1 and 0.4. The
248 correlation length σ is defined to be of the same size of the cells used for the initial
249 tomographic scheme, that is 25 km.
250 Finally, we chose the value of α based on the variation of the penalty function with α ('L-
251 curve'). Our preferred value of α was chosen to be near the maximum curvature of the
252 L-curve.
253 Figure 6 shows the group velocity maps at 3, 8, 10 and 15 sec period. At 3 sec period, a
254 high velocity anomaly is present in northeastern corner of the model while the central
255 part of the map is dominated by homogeneous velocities. The limit of the high velocity
256 anomaly coincides with the edge of the Lapland Granulite Terrane ('LGT'). At 5 (fig. 6-b)
257 and 8 (fig. 6-c) sec period, the LGT is still present even though the velocity variations are
258 smaller than at 3 sec period. At 15 sec period, the LGT is still visible, but with a small
259 amplitude and shifted towards the NE.
260 The spatial resolution of the tomographic model was calculated using the method by
261 Barmin et al. (2001). Figure 7 show the spatial resolution for the group velocity map at 5
262 sec period. The maximum resolution is better than 50km in the center of the array. The
263 resolution decreases towards the edge of the array. We will subsequently invert the
264 group velocity maps in areas with a resolution better than 100km, but over most of the
265 model the resolution is better than 50 km.
266
267 **4.-3D Vs MODEL**
268 Starting from the group velocity maps, we extracted a dispersion curve at each point of
269 the model. All dispersion curves were then inverted to obtain S wave velocity, using a
270 linearized inversion scheme (Hermann and Ammon, 2006). By combining the 1-D Vs(z)
271 profiles we obtain a 3D Vs model.

272

273

274

275 **4.1-Depth Vs inversion**

276 Prior to the inversion at each grid point, we inverted the average group velocity
277 dispersion curve (fig 8-a) to define an average crustal Vs structure for the region (fig 8-
278 b). During this inversion we used as input a slightly modified version of the model
279 proposed by Poli et al. (2012). The difference resides in the discretisation of the upper
280 crust, for which Poli et al. (2012) did not have any resolution. We discretized the upper
281 crust (down to 28 km depth) using 17 layers, of varying thickness from 1 km to 5 km as
282 function of depth. Between 28 km depth and Moho, at 46 km depth, we use a single layer
283 of 18 km thickness.
284 With the limited depth resolution of the fundamental mode Rayleigh waves, we impose
285 smooth velocity variations with depth within the top 17 layers. The velocity is allowed
286 to take a large range of values (± 0.2 km/sec) as long as the depth variation is smooth.
287 This will lead, within the given model parametrisation, to a very well defined solution.
288 We only allowed for small velocity variations (± 0.02 km/sec) in the thick lowermost
289 crustal layer while mantle velocities were kept constant at a value of 4.54 km/s. We
290 verified that these constraints on the deep structure did not significantly change the
291 upper crustal structure. In view of the subsequent inversion for Vs(z) in each grid point,
292 we verified that small to moderate errors in Moho depth (± 5 km) did not influence the
293 upper crustal structure.
294 The average model of figure 8-a was used as starting point for the inversion in each grid
295 point. Even though the influence on upper crustal structure is negligible, we adapted
296 Moho depth at each point using results from a receiver function study based on the

297 LAPNET array (Silvennoinen et al., in prep.). Depth constraints were the same as those
298 imposed for the inversion of the average dispersion curve. The data fit was good for all
299 the grid points. The average data misfit over all grid points and periods is 0.01 km/sec.

300 **4.2-Vs maps and sections**

301 Our 3D shear velocity model is presented in figure 9 as horizontal slices at different
302 depths and vertical cross sections. The overall velocity variations are smaller than ±3%
303 with respect to the average velocity model, with lateral variations mainly present in the
304 upper crust, in agreement with Janik et al. (2009). Due to the limited period interval, we
305 will here focus our discussion to the upper 25 km of the crust. The main features of the
306 Vs-model are the body of high velocities in the NE corner (up to +2.5%) and a less
307 pronounced low velocity anomaly (reaching up to -1.5%), most pronounced towards the
308 SE.

309 The limit of the dominating high Vs anomaly coincides at surface with the edge of the
310 Lapland Granulite Terrane (LGT). The lower limit of the high velocity body is almost
311 vertical at the edge, flattens at approximately 10-15km depth, and finally dips more
312 steeply towards the N-NE. Despite limitations in our resolution, we observe that this
313 geometry is in excellent agreement with results from an active seismic experiment
314 approximately located along profile B-B' (e.g. Janik et al. 2009), while our results
315 additionally provide insight on the 3-D geometry of the interface.

316 The southern low velocity anomaly does not bear direct link to the surface geology. On
317 the other hand, within the same geological units (Karajok-Kittila Greenston Belt, Central
318 Lapland Complex, Granitoid Complex), we observe resolved differences between the low
319 velocity anomaly towards the south, and slightly higher velocities in the western part of
320 the study area. The low velocity anomaly dips down beneath the high velocity body

associated with the LGT. Our results are therefore compatible with recent tectonic models by Daly et al. (2006) and Janik et al. (2009).

5- CONCLUSIONS

Ambient Noise Tomography here provides constraints on the 3-D geometry of the Archean-Proterozoic contact in northern Finland, as defined at the surface by the edge of the Lapland Granulite belt. Our tomography is in agreement with recent active seismic imaging and tectonic models which imply a north oriented subduction as proposed by Daly et al. (2006) and Janik et al. (2007). Our results demonstrate the value of ANT for seismic imaging also in areas with very small lateral velocity variations, such as cratons. The robustness of the imaging is dependent upon careful correlation processing and analysis of the noise field. The use of short time windows (Prieto et al., 2011; Poli et al., 2012; Seats et al., 2012; this work) seems particularly adequate to improve the estimate of the Green's function, as it is possible to reject high amplitude signals without strongly decreasing the amount of data. With this approach it is no longer necessary to apply any time normalization such as 1-bit processing or dividing by the moving average of the signal amplitude. An additional advantage is that the output correlations are broadband, so it is relatively easy to retrieve a reliable and continuous group velocity dispersion curve.

To confirm the strong benefit of our processing, a presence of homogeneous coherent noise energy is systematically observed over all azimuths. Comparison between Rayleigh and Love waves yield compelling results that are not yet understood. A first important point is the complex behavior observed for short period Love waves. TT components are dominated by a mix of higher modes which could possibly be

346 interpreted as Lg waves. Even though we cannot yet provide a satisfactory explanation
347 for the observations, our results indicate that ANT cannot automatically be applied to
348 the TT component of correlations at this stage.
349 Concerning the noise distribution, we observe that energy is incoming for similar
350 azimuths for the two types of waves, but the amplitude is different between Rayleigh
351 and Love waves. Noise generation of Rayleigh waves can be explained in terms of
352 vertical pressure variations induced by nonlinear wave-wave interaction between ocean
353 gravity waves (Longuet-Higgins, 1950, Hillers et al., 2012). This mechanism is not
354 directly applicable to the generation of Love waves. Love waves are excited in presence
355 of horizontal forces (Fukao et al., 2010, Saito, 2010), as can be generated in presence of
356 strong bathymetric variability. The difference in azimuthal energy distribution could
357 explain how is different the sea bottom topography of source regions and how the
358 planar bottom assumptions (Longuet-Higgins, 1950) is inappropriate to model the
359 generation of seismic noise.
360

361 **ACKNOWLEDGEMENT**

362 We greatly acknowledge support from the QUEST Initial Training network funded
363 within the EU Marie Curie Programme. This study received supported from the ANR
364 BegDy project, the Institut Paul Emil Victor, and European Research Council through the
365 advanced grant “Whisper” 227507. We thank N. Arndt for useful discussions. The
366 POLENET/LAPNET project is a part of the International Polar Year 2007-2009 and a
367 part of the POLENET consortium, and received financial support from The Academy of
368 Finland (grant No. 122762) and University of Oulu, ILP (International Lithosphere
369 Program) task force VIII, grant No. IAA300120709 of the Grant Agency of the Czech
370 Academy of Sciences, and the Russian Federation : Russian Academy of Sciences

(programs No 5 and No 9). The Equipment for the temporary deployment was provided by: RESIF – SISMOB, FOSFORE, EOST-IPG Strasbourg Equipe sismologie (France), Seismic pool (MOBNET) of the Geophysical Institute of the Czech Academy of Sciences (Czech Republic), Sodankyla Geophysical Observatory (FINLAND), Institute of Geosphere Dynamics of RAS (RUSSIA), Institute of Geophysics ETH Zürich (SWITZERLAND), Institute of Geodesy and Geophysics, Vienna University of Technology (AUSTRIA), University of Leeds (UK). POLENET/LAPNET data were prepared and distributed by the RESIF Data Center. The POLENET/LAPNET working group consists of: Elena Kozlovskaya, Teppo Jämsen, Hanna Silvennoinen, Riitta Hurskainen, Helle Pedersen, Catherine Pequegnat, Ulrich Achauer, Jaroslava Plomerova, Eduard Kissling, Irina Sanina, Reynir Bodvarsson, Igor Aleshin, Ekaterina Bourova, Evald Brückl, Tuna Eken Robert Guiguet, Helmut Hausmann, Pekka Heikkinen, Gregory Houseman, Petr Jedlicka, Helge Johnsen, Elena Kremenetskaya, Kari Komminaho, Helena Munzarova, Roland Roberts , Bohuslav Ruzek, Hossein Shomali, Johannes Schweitzer, Artem Shaumyan, Ludek Vecsey, Sergei Volosov.

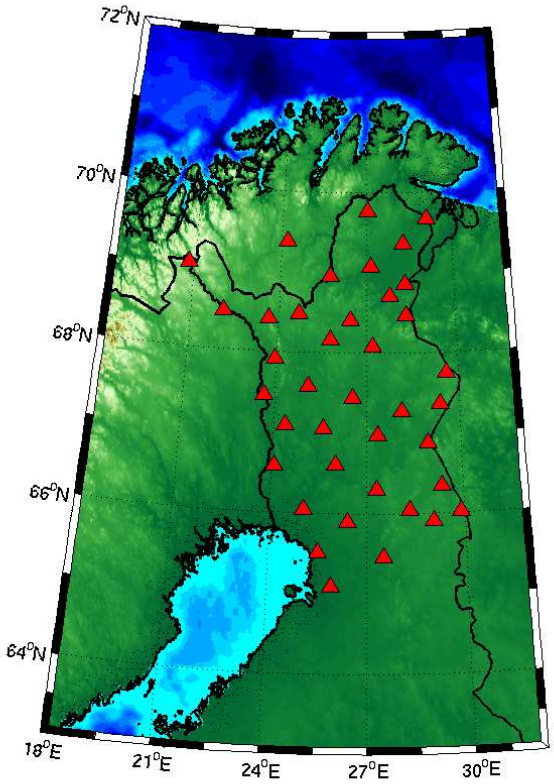

387

388 Fig 1: Map of the study area: red triangles are the seismic stations.

389

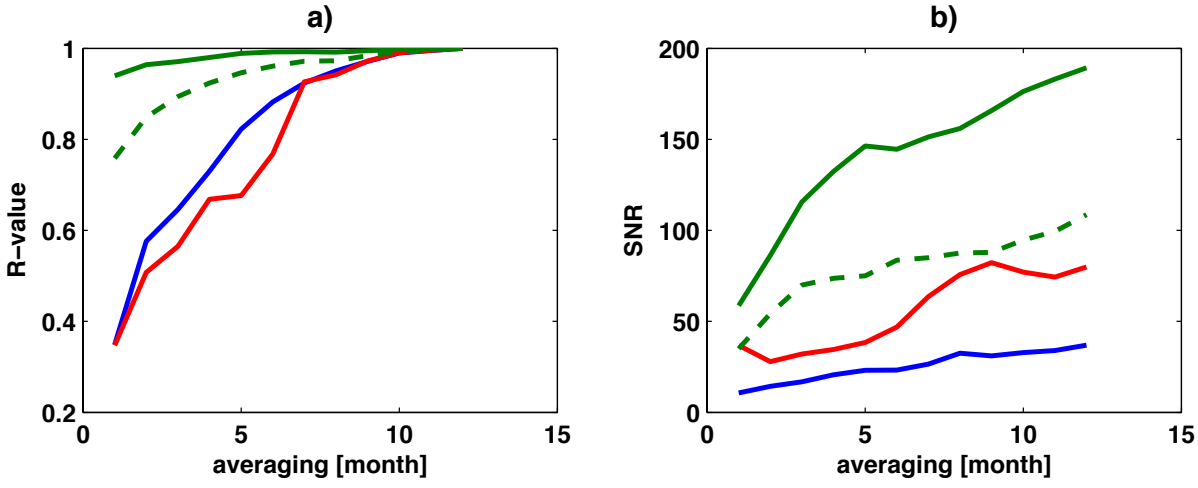

390

391 Figure 2: comparison of the different processing: a) R-value as function of time

392 averaging for processing as in Poli et al. (2012) using 4 hours windows (green solid

393 line), 24 hours windows (green dashed line), one-bit correlation with hours windows

394 (blue line) and linear correlation with 4 hours windows (red line). b) SNR as function of

395 time averaging. Color code is the same of a).

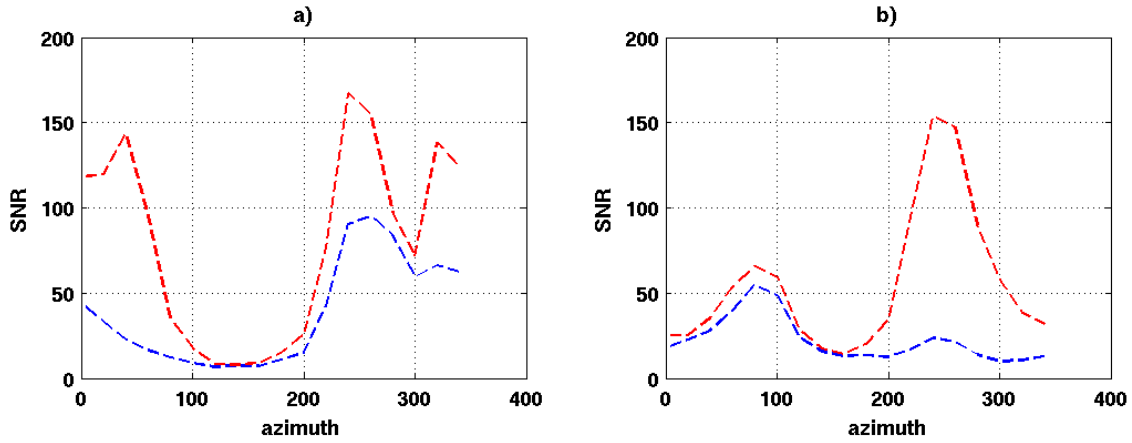

396

397

398 Fig 3: SNR as function of azimuth for the period range a) 20-10 sec b) 10-2 sec. Red

399 dashed lines represent Rayleigh waves, blue dashed lines Love waves.

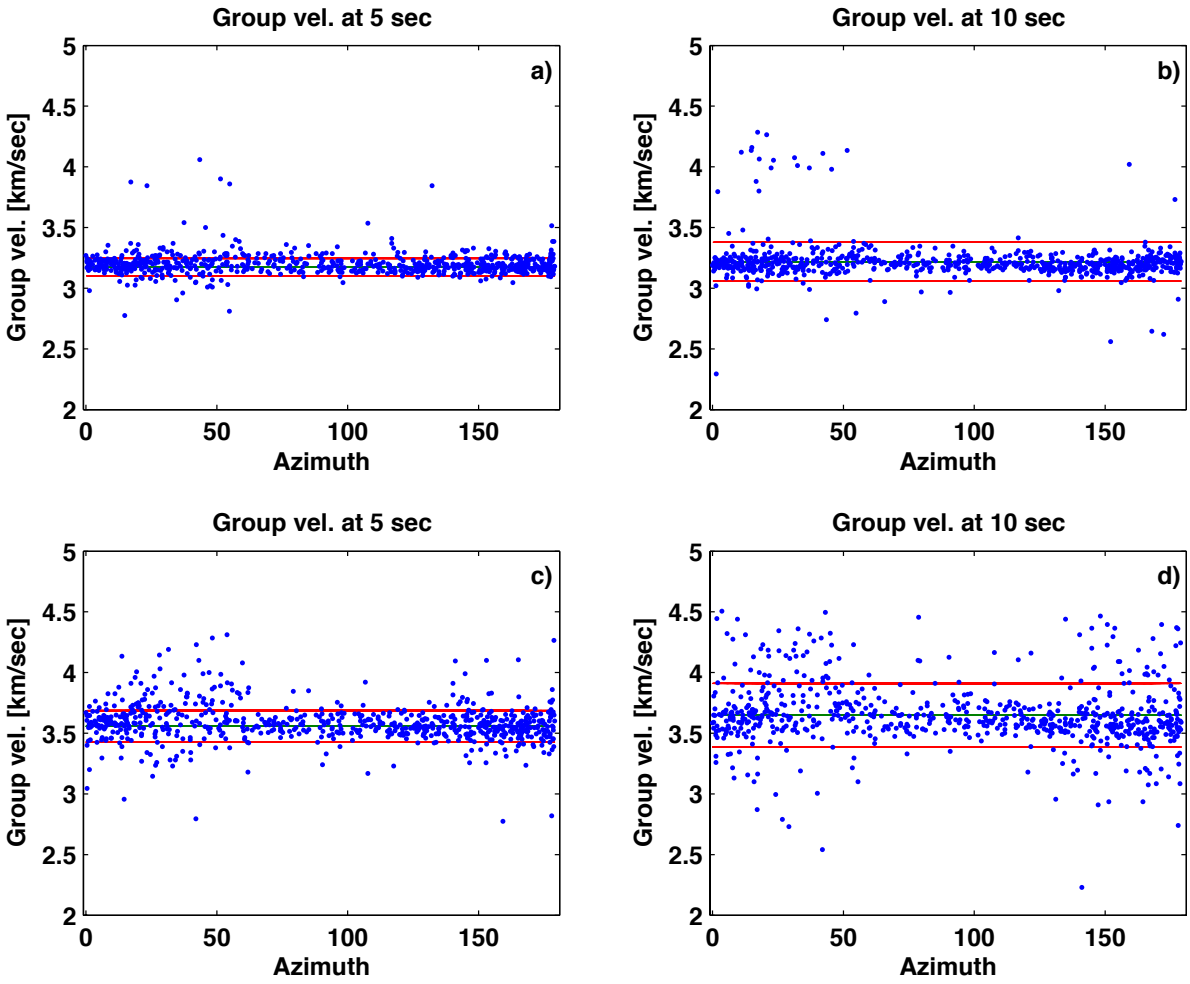

400

401 Fig. 4: azimuthal distribution of measured group velocity for Rayleigh waves (a-b) and

402 Love waves (c-d). Red lines are the velocity standard deviation and green lines

403 represents the average group velocity.

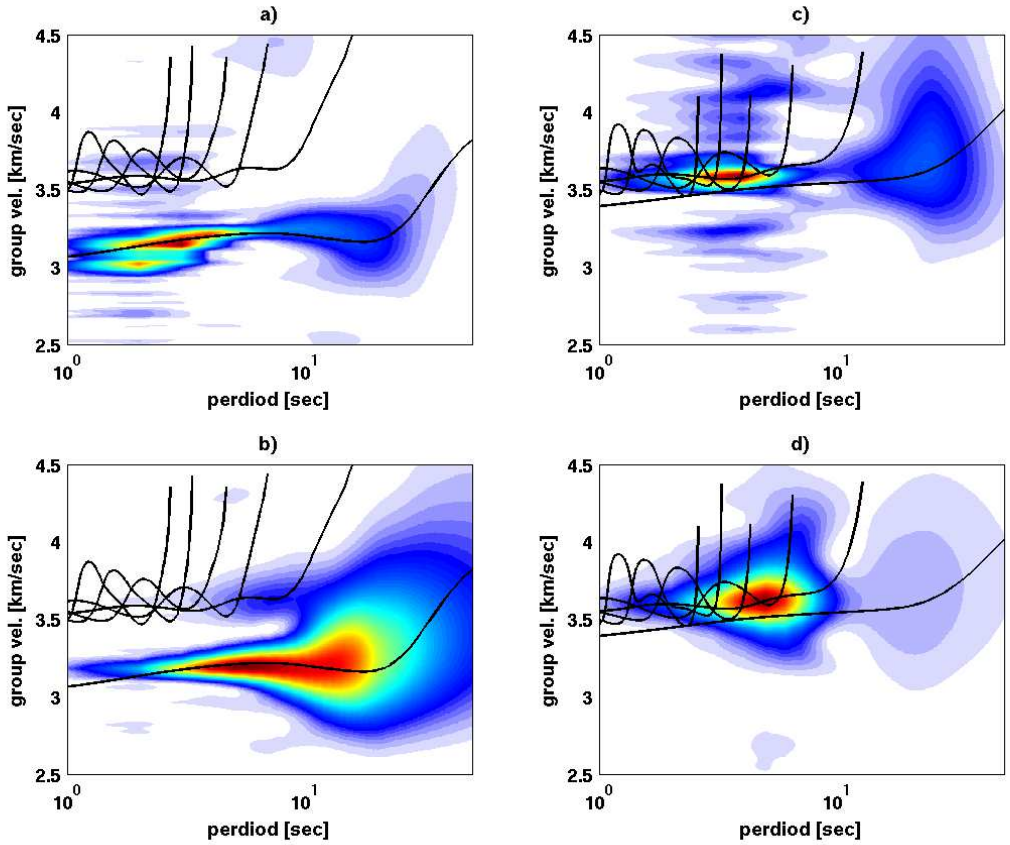

Fig 5: example of dispersion measurement for a couple of station separated about 500 km apart. a) ZZ components spectrogram, with the dispersion curves of the firsts five Rayleigh wave modes, b) TT spectrogram with the dispersion curves of the firsts five Love wave modes. Dispersion curves were calculated starting for an average crustal model of the area (fig. 6).

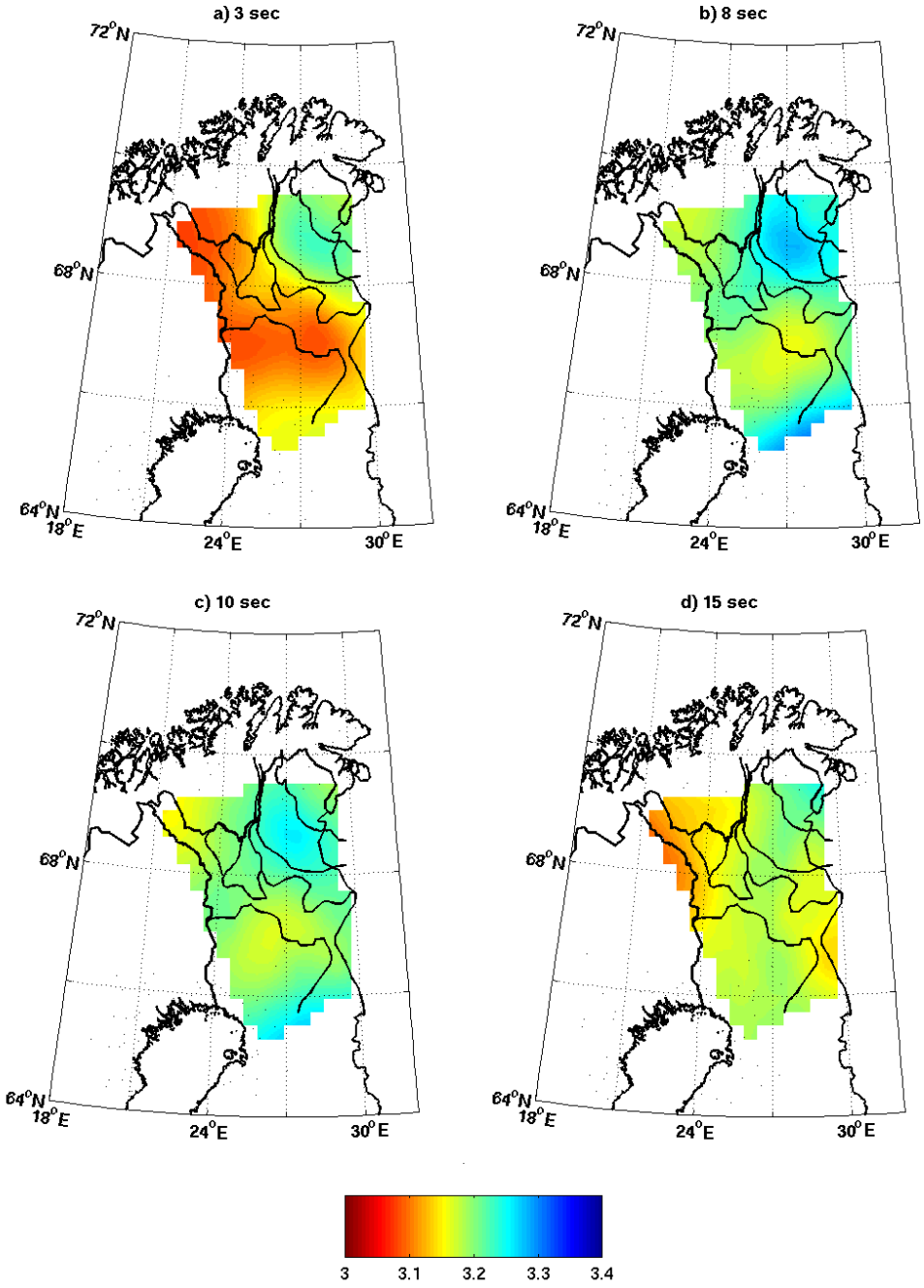

411

412

413 Fig 6: group velocity map for different periods (indicated over each map). Black lines are

414 the limits of the major geological units of the area. Colorbar is the group velocity in

415 km/sec. For the names of geological units see figure 9.

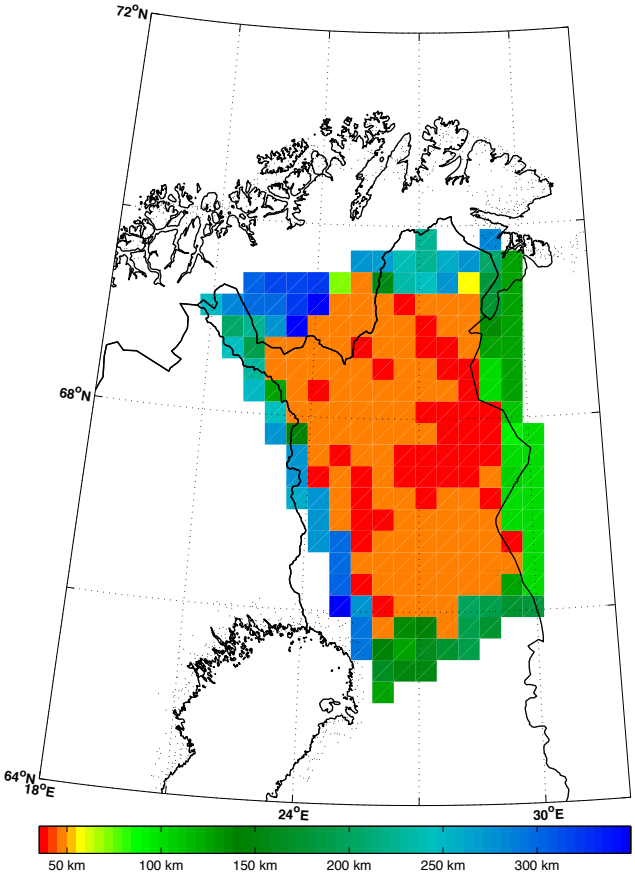

Figure 7: resolution map for 5 sec period Rayleigh waves group velocity model.

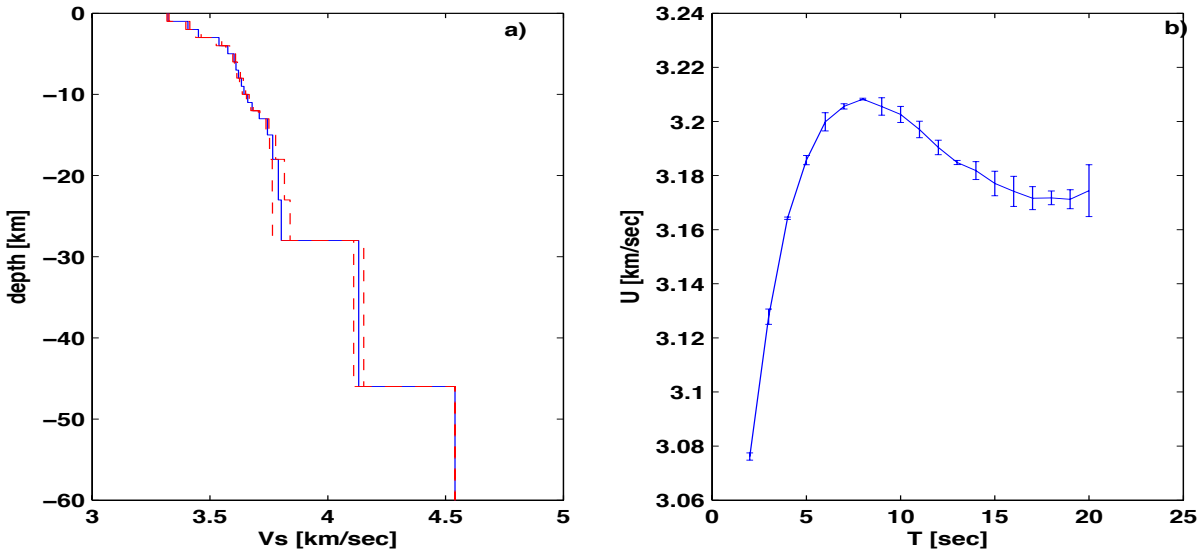

Figure 8: a) average shear velocity model of the area with the associated variance (red dashed lines). b) average dispersion curve and the associated error relative to the theoretical curve of the inverted model.

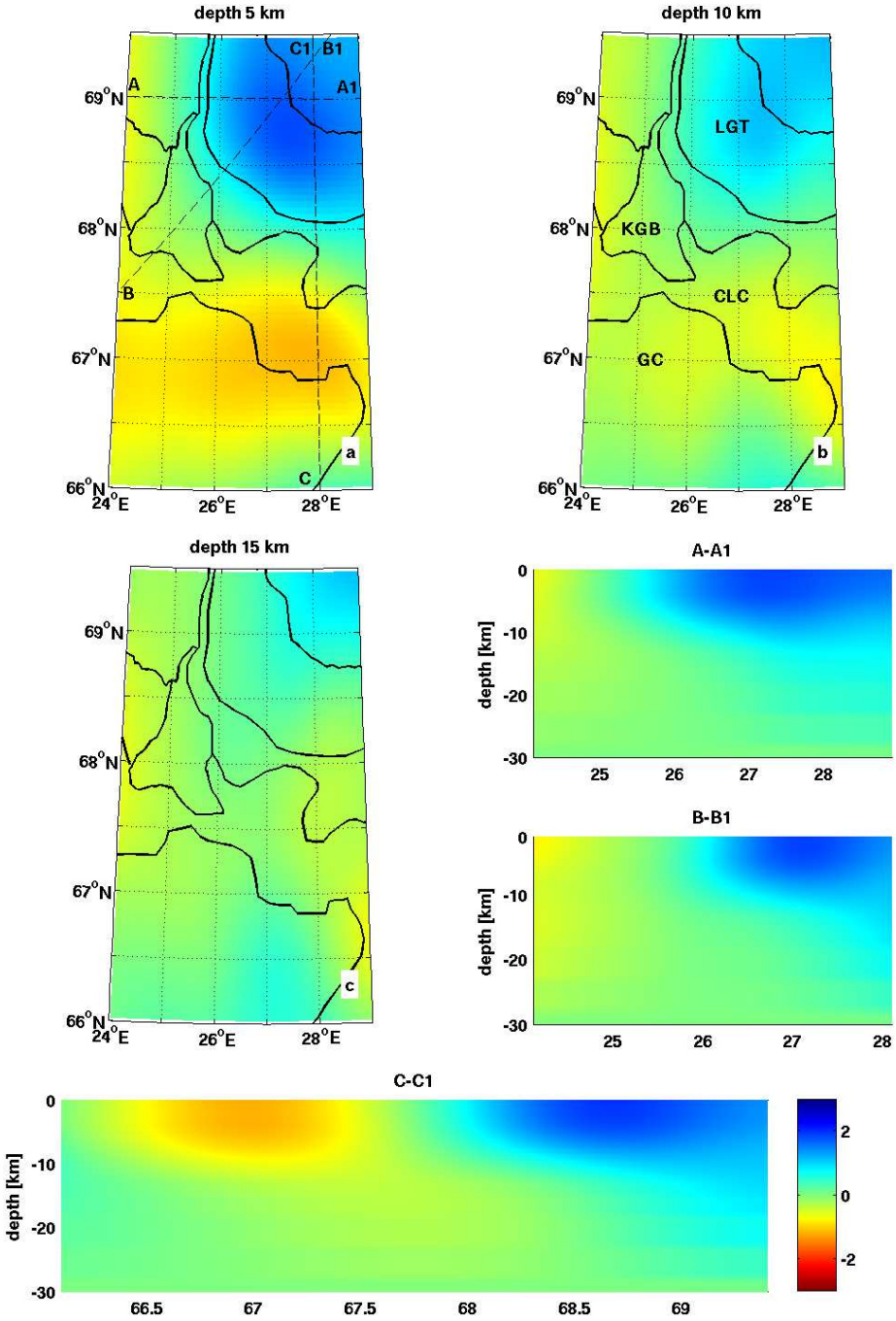

423

424 Figure 9: Vs velocity maps at 5 a), 10 b) and 15 km c) of depth. Dashed lines in figure a)

425 are the geographical location of the sections. The major geological limits are plotted over

426 each maps and the relative name of the geological units is in figure b). Colorbar is the

velocity variation in % respect to the average model. LGT Lapland Granulite Terrane, KGB Karasjok-Kittila Greenstones Belt, CLC Central Lapland Complex, GC Granitoid complex.

REFERENCES

Barmin, M. P., Ritwoller, M. H. and Levshin, A. L., 2001, A Fast and Reliable Method for Surface Wave Tomography, *Pure and Applied Geophysics,* **158**, 1351-1375

Campillo, M, 1990, Propagation and Attenuation of Crustal Phase Lg, *Pure and Applied Geophysics,* **132**

Campillo, M and Paul, A., 2003, Long-range correlations in the diffuse seismic coda; *Science,* **299,** 547-549.

Daly, J. S., Balagansky, V. V., Timmerman, M. J. and Whitehouse, M. J., 2006, The Lapland-Kola orogeny: Paleoproterozoic collision and accretion of the northern fennoscandian lithosphere; in *European Litosphere Dynamics*, *Geol. Soc. Of London Mem. Ser.*, **32**, 579-598.

Friederich, A., Kruger, F. &Klinge, K.,, 1998, Ocean-generated microseismic noise located with the Gräfenberg array, *J. Of Seism.* **2,**47-64.

451 Froment, B., Campillo, M., Roux, R., Gouédard, P., Verdel, A. and Weaver, R. L., 2010,
452 Estimation of the effect of nonisotropically distributed energy on the apparent arrival
453 time in correlations, *Geophysics*, **75,**
454
455 Fukao, Y., Nishida, K. and Kobayashi, N., 2010, Seafloor topography, ocean infragravity
456 waves, and background Love and Rayleigh waves, *J. Geophys. Res.*, **115**.
457
458 Gouédard ,P., Stehly, L., Brenguier, F., Campillo, M., de Verdiére, Y. C., Larose, E.,
459 Margerin, L., Roux, P., Sànchez-Sesma, F. J., Shapiro, N. M., & Weaver, R. L., 2008,
460 Cross-correlation of random fields: mathematical approach and applications, *Geophys.*
461 *Prospect.*, **56**, 375–393.
462
463 Herman, R. B. and Ammon, C. J., 2002, Surface waves, receiver function and crustal
464 structure, St. Louis University.
465
466 Hillers, G., Graham, N., Campillo, M., Kedar, S., Landés, M. and Shapiro, N., 2012, Global
467 oceanic microseism sources as seen by seismic arrays and predicted by wave action
468 models, *Geochem. Geophys. Geosyst.*, **13**
469
470 Janik, T., Kozlovskaya, E & Yliniemi , J., 2009, Crust-mantle boundary in the central
471 fennoscandian shield: Constraints from wide-angle p and s wave velocity models and
472 new results of reflection profiling in Finland, *J. Geophys. Res.*, **112**.
473

Kohler, A., Widle, C. & Maupin , V., 2011, Directionality analysis and Rayleigh wave tomography of ambient seismic noise in southern Norway, *Geophys. J. Int.*, **184**, 287-300.

Kozlovskaya, E, Poutanen, M. & P. W. Group. POLENET/LAPNET- a multi-disciplinary geophysical experiment in northern fennoscandia during IPY 2007-2008, 2006, Geophysical research abstract.

Levshin, A., Yanovskaya, T., Lander, A., Buckin, B., Barmin, M., Ratnikova, L., & Its, E., 1989, Seismic surface waves in a Laterally inhomogeneous Earth, ed. Keilis-Borok, VI, Kluwer, Norwell, M.A.

Longuet-Higgins, M. S., 1950, A theory of the origin of microseisms; *Philos. Trans. R. Soc. London*, Ser. A, **243**, 1-35

Pedersen H., Kruger, F & the SVEKALAPKO Seismic tomography, 2007, Influence of the seismic noise characteristics on noise correlations in the Baltic shield, *Geophys. J. Int*, **168**, 197-210.

Poli, P., Pedersen, H. A., Campillo, M. & Polenet Lapnet working group, 2012, Emergence of body waves from cross-correlation of seismic noise, *Geophys. J. Int*, **188**, 549-558.

Prieto,G. A., Denolle, M. Lawrence, J. F. & Beroza, G. C., 2011, On the amplitude information carried by ambient seismic field, *Compte Rend. Geosc.*, **3**, 558–570.

Ritzwoller, M. H., Lin F. & Shen, W., 2011, Ambient noise tomography with a large seismic array, *Compte Rend. Geosc.*, **3**, 558–570.

Sabra, K. G., Gerstoft, P., Roux, P. and Kuperman, W. A., 2005a, Extracting time-domain Green's function estimates from ambient seismic noise, *Geophys. Res. Lett*, **32**.

Sabra, K. G., Gerstoft, P., Roux, P., Kuperman, W.A. & Fehler, M. C., 2005b, Surface wave tomography from microseisms in southern california. *Geophys. Res. Lett*, **32**.

Saito, T., 2010, Love-wave excitation due to the interaction between a propagating ocean wave and sea-bottom topography, *Geophys. J. Int*, **182** 1515-1523.

Seats, K. S., Lawrence, F. J., & Prieto, A. P., 2011,Improved ambient noise correlations function using Welch's method, *Geophys. J. Int*, **188**, 513-523.

Shapiro, N. M. & Campillo, M.,2004, Emergence of broadband rayleigh waves from correlations of the ambient seismic noise, *Geophys. Res. Lett*, **31**.

Shapiro, N.M, Campillo, M., Stehly, L. & Ritzwoller, M. H., 2005, High-Resolution Surface-Wave tomography from ambient seismic noise. *Science*, **307**, 1615 –1618.

Silvennoinen, H., Kozlovskaya, E., Kissling, E., Kosarev, G. & POLENET/LAPNET Working Group, 2012, Compilation of moho boundary for northern fennoscandia, submitted.

Stehly, L., Campillo, M. & Shapiro N.M., 2006, A study of the seismic noise from its long-range correlation properties. *J. Geophys. Res.*, **111**, 1615 –1618.

Stehly, L., Fry, B., Campillo, M., Shapiro, N., Guilbert, J., Boschi, L. & Giardini, D., 2009, Tomography of the Alpine region from observations of seismic ambient noise, *Geophys. J. Int*., **178**(1), 338-350.

Yao, H. & van der Hilst, R., 2009, Analysis of ambient noise energy distribution and phase velocity bias in ambient seismic noise tomography, with application to SE Tibet, *Geophys. J. Int.*, **179**, 1113-1132.

Zhan, Z., Ni, S., Helmberger, D. V., & Clayton, R. W., 2010, Retrieval of moho-reflected shear wave arrivals from ambient seismic noise, *Geophys. J. Int.*, **1**, 408-420.